1   **New Insights into the Conformational Activation of Full-Length Integrin**

2

3   Tamara C. Bidone[1], Anirban Polley[1,#], Aleksander Durumeric[1], Tristan Driscoll[3], Daniel
4   Iwamoto[4], David Calderwood[4], Martin A. Schwartz[2,3], Gregory A Voth[1]*

5

6   [1]Department of Chemistry, Institute for Biophysical Dynamics, and James Franck Institute, The
7   University of Chicago, 5735 S. Ellis Ave., Chicago, Illinois 60637, USA.

8   [2]Yale Cardiovascular Research Center and Department of Internal Medicine (Section of
9   Cardiovascular Medicine)

10   [3]Departments of Cell Biology and Biomedical Engineering, Yale University, New Haven,
11   Connecticut 06511, USA.

12   [4]Department of Pharmacology, Yale University, New Haven, Connecticut 06511, USA

13   [#]*present address*: Department of Chemical Engineering, Columbia University, New York City

14
15   * corresponding author: gavoth@uchicago.edu
16
17

18   **ABSTRACT**

19

20   Integrin binding to extracellular matrix proteins is regulated by conformational transitions from
21   closed, low affinity states to open, high affinity states. However, the pathways of integrin
22   conformational activation remain incompletely understood. Here, by combining all-atom
23   molecular dynamics simulation, coarse-graining, heterogeneous elastic network modeling, and
24   experimental ligand binding measurements, we test the effect of integrin β mutations that
25   destabilize the closed conformation. Our results support a "deadbolt" model of integrin
26   activation, where extension of the headpiece is not coupled to leg separation, consistent with
27   recent cryo-EM reconstructions of integrin intermediates. Moreover, our results are inconsistent
28   with a "switchblade-like" mechanism. The data show that locally correlated atomistic motions
29   are likely responsible for extension of integrin headpiece before separation of transmembrane
30   legs, without persistence of these correlations across the entire protein. By combining modeling
31   and simulation with experiment, this study provides new insight into the structural basis of full-
32   length integrin activation.

33

34

INTRODUCTION

Integrins are transmembrane receptors that signal bidirectionally across the plasma membrane to regulate cell processes such as adhesion, migration, differentiation, and mechanosensing (1–6). Integrins can be found in either bent conformations that bind to extracellular matrix (ECM) ligands with low affinity or in open, high affinity conformations (6–9). The structure of integrin resembles a large head and two legs, with the head containing sites for ligand binding. Both head and legs comprise several subdomains, interconnected by linkers. Owing to the large dimensions of the receptor and the complex interconnections between and within subdomains, that determine activation state, how integrin transits from bent to extended conformations is not totally understood.

Integrins are heterodimers composed of an α and a β subunit that associate non-covalently. For integrin αvβ3, the two subunits form a structure with an extracellular ligand-binding headpiece, two transmembrane helices and two short cytoplasmic tails (10) (Figure 1). The αv subunit consists of five extracellular domains: a seven-bladed β-*propeller* and a *thigh* domain, which is connected by the flexible *linker 1* to the *calf* domains, followed by the *transmembrane* and *cytoplasmic* or *tail* domains. The β3 subunit has seven domains with flexible interconnections: the *βA domain* is inserted into the *hybrid* domain, which is, in turn, inserted in the *plexin-semaphorin-integrin* (PSI) domain; these domains are followed by four cysteine-rich *epidermal growth factor* (EGF) modules and the *cytoplasmic* domain (11). The structure of the bent, low affinity integrin αIIbβ3, which is closely related to αvβ3, is represented in Figure 1a.

Integrin activation occurs via a large scale conformational rearrangement involving relative motions between the α and β subunits and their subdomains on the order of nanometers. Previous studies showed that localized changes of the βA/hybrid interface of the β subunit of both αIIbβ3 and αvβ3 integrins, are critical for these movements (12–14). For example, the α7 helix of the βA domain shifts towards the hybrid domain in a piston-like movement that causes the hybrid domain to swing out by ~60° (8, 15, 16). Also, upon activation, Glu318 in the α subunit β-*propeller* domain becomes bound to the β subunit βA metal site (15, 17). These localized rearrangements in the integrin headpiece shift the conformation from bent to open (8, 12–14). Molecular dynamics (MD) simulations on αvβ3, in combination with steered molecular dynamics (SMD) studies, have suggested that inter-domain contacts between the legs and headpiece raise the energy barrier that must be overcome for opening the βA/hybrid hinge (18). Therefore, concomitantly with the reorganization of both α and β subunits in the integrin headpiece, opening of αvβ3 involves breaking the extensive interfaces between the headpiece and lower legs, and this is valid also for $\alpha_{IIb}\beta_3$ (12).

Integrin activation also requires separation of the transmembrane legs. Previous work has studied the initiation of integrin opening by focusing on segments of the integrin headpiece at the nanosecond timescale (19). Less is known about how headpiece motions coordinate with leg separation, which occurs on the second timescale. In fact, several studies of integrin activation examined proteins with mutated, truncated, or entirely absent legs, thus preventing this kind of analysis (16, 20–22).

80   In order to explain the intrinsically multiscale mechanism of integrin opening, two conceptual
81   models based on experimental observations have been proposed. In the "switchblade" model (8),
82   opening of the βA/hybrid hinge and separation of transmembrane legs occur in a coordinated
83   fashion. In contrast, the "deadbolt" model proposes more conservative changes around the bent
84   structure with progressive loss of constraining contacts between βA domain and β tails that occur
85   before leg separation (23). Thus, without dynamic, nonequilibrium information about how
86   structural changes in the headpiece are coupled to the separation of the legs, major questions
87   remain concerning the pathway of integrin opening.
88
89   Recently, structures captured in various degrees of opening of full-length $\alpha_{IIb}\beta_3$ integrin showed
90   headpiece extension without leg separation (24). However, even in this scenario, it is still
91   possible that electrostatic interactions in the β_3 helix decrease upon headpiece extension and that
92   a coordinated structural change occurs at the interface between the two legs without detectable
93   separation, consistent with coordinated structural reconfiguration between headpiece and legs at
94   short length and time scales.
95
96   In order to understand the relationship between headpiece extension and legs separation, we have
97   combined here a multiscale simulation approach with experimental ligand binding
98   measurements. We tested the effect of activating mutants on the molecular structure and their
99   impact on the long-range structural rearrangements of integrin. Our results support the notion
100   that headpiece extension occurs before legs separation, consistent with a deadbolt model of
101   integrin activation and inconsistent with a switchblade model. This mechanism is mediated by
102   local, correlated atomistic motions within and between neighboring subdomains of the receptor,
103   and independent from long-range interactions.
104

105 **RESULTS**

106 **All atom molecular dynamics simulations of integrin mutants**
107 Inspections of root mean square deviation (RMSD) plots of WT, single, and double integrin
108 mutants showed that all structures reached local equilibrium states within 1 μs of MD
109 simulations (Figure 2a,d). Analysis of root mean square (RMS) fluctuations also showed that
110 some of the most flexible regions of integrin are at the interface between the β-propeller and βA
111 domains, together with the Linker 1 and EGF motifs, which form the α and β genu, respectively
112 (Figure 2b-c, e-f). There was no significant difference in RMS fluctuations between WT and the
113 mutant integrins considered here. These data collectively support that the EGF domain region is
114 relatively plastic, especially between EGF1 and EGF2, at the β knee, and at the PSI/hybrid and
115 hybrid/I-EGF1 junctions. It was previously reported that the flexibility of the βA domain would
116 also facilitate such interdomain interactions (15).

117
118 Over the last 100 ns of the AA MD simulations, the average angle $< \vartheta >$ of the mutants was
119 about 5-7% different from WT (Figure 3b); D_{12} was enhanced in the S243E mutant relative to
120 both WT and other single/double mutants (figure 3c); D_{EM} was about 15% different for the single
121 mutants and about 8% different in the double mutants relative to WT (Figure 3d). Accordingly,
122 the single mutants showed enhanced persistency of high values of D_{EM} (Figure 3e). Time
123 evolution of D_{12}, D_{EM}, and corresponding probability distributions, are reported in Figure S1 and
124 FigureS2 of the Supplemental Information. Time evolutions of ϑ_1 and ϑ_2 are reported in Figure
125 S3. Both maximum values and standard deviations of ϑ_1 and ϑ_2 over the 1μs-long MD
126 simulations were higher in S243E mutant than the other integrin single/double mutants (Figure
127 S4a-b). Maximum value and standard deviation of ϑ_1, over 1μs-long MD, were among the
128 highest for D723R with respect to the other single mutants (Figure S4a-b). High standard
129 deviations in the kink angles of S243E and D723R with respect to the other single mutants
130 indicate that the configurations of the two headpiece hinges were far from their mean. Thus, the
131 angles were more flexible in these mutant relative to the other single mutants examined. Also,
132 maximum value and standard deviation for D_{12} were higher in the S243E and D723R (Figures
133 S4c) relative to the other single mutants. Among the double mutants, D723R-E206T also showed
134 high values of peak and standard deviation for kink angle, leg separation, and headpiece
135 extension (Figure S4a-d). Taken together, these results support that the mutants here tested
136 destabilize the integrin closed conformation by enhancing variability of kink angles in both
137 subunits, leg separation, and/or overall distance of the headpiece from the transmembrane legs.

138
139 We next addressed the molecular mechanism by which S243E, one of the most activating
140 mutant, affects integrin conformation. In WT integrin, neutral histidine 244, negatively charged
141 aspartic acid 113, and positively charged arginine 352 surround S243, with Arg352 at a distance
142 (Figure 4a). In MD simulations of systems with protonated glutamic acid in S243E, a salt-bridge
143 formed between the oxygen atom of arginine and the hydrogen atom of glutamic acid (Figure
144 4b). Salt bridge formation was accompanied by reorientation of the positively charged arginine,
145 which moved closer to the negative charged glutamic acid and re-oriented towards the negatively
146 charged aspartic acid (figure 4b). These molecular rearrangements resulted in greater headpiece
147 extension, flattening of kink angles and separation of the transmembrane legs in the MD
148 simulations. Time evolution and probability density functions of distances of ARG352 from the
149 center of mass of residues 244, 243 and 113 in WT and mutant conditions are in Figure S5.

150

151 Taken together, the analysis of MD simulations showed local destabilization of the closed
152 configuration in integrin mutants. However, structural quantities which are representative of
153 integrin conformational activation at the level of the whole receptor, such as D_{EM}, ϑ_1 and ϑ_2, did
154 not convergence within 1 μs. In order to allow for enhanced sampling of integrin long-range
155 interactions, we instead used the MD trajectories to build CG models.

156

157 **Coarse-grained (CG) simulations**
158 Atomistic integrin structures were converted into CG systems, without the lipid bilayer included
159 explicitly in the CG model, to detect large-scale motions of the receptor. As described earlier, we
160 used a combination of ED-CG and heteroENM to create the CG model and systematically
161 removed harmonic bonds or converted them into Morse potentials, motivated by the assumption
162 that weak CG effective harmonic correlations between domains are likely to dissociate upon
163 integrin activation. We analyzed our results to identify structural differences between WT and
164 mutant integrins. Our goal was to sample multiple integrin states underlying the equilibrium
165 conformers and to provide insight concerning which mutants most potently destabilize integrin
166 closed states. We mapped the atomistic WT system to a CG ED-CG model of 200 CG sites or
167 "beads", with average resolution 8 ± 3 residues per CG site, which is of the same order used
168 previously (32). We compared the CG root mean square fluctuations from ED-CG-heteroENM at
169 different initial cutoffs, spanning 3-5 nm, with those from atomistic simulations converted into
170 CG fluctuations (Figure 5a). Using cutoffs of 3, 4, or 5 nm, the average differences in RMS
171 fluctuations from the all-atom fluctuations were 0.11, 0.12 and 0.16 nm, respectively. We
172 therefore chose a 3 nm cutoff for our CG systems that best reproduced atomistic fluctuations, and
173 built ED-CG-heteroENM models for each mutant integrin (Figure 5b). The fraction of intra-
174 domain springs was about 0.6 in all systems, with inter-domain springs that connected non-
175 consecutive subdomains along the primary sequence below 0.2. Intra-domain connections had
176 the highest spring constants, up to 25 kcalmol^{-1}A^2 (Figure 5d), while inter-domain springs had
177 about 3-fold lower characteristic spring constants, below 8 kcalmol^{-1}A^2 (Figure 5e-f). Snapshots
178 from a representative CG simulation showed average kink angles between 120-140 deg (Figure
179 6a), depending on the particular mutant. Theses angles are about twice those from MD, showing
180 that conformations far from equilibrium were sampled with this CG method and that the
181 structures are extended. All mutants showed higher kink angles than WT αvβ3 (Figure 6a). Also,
182 comparison of the fraction of time that D_{EM} is above 95% of its maximum showed that all the
183 mutants were above 15%, whereas WT integrin was below 10% (Figure 6b). Thus, in the CG
184 simulations, the mutants were in extended conformations more often than WT. By capturing the
185 effect of point mutations, our CG models of integrin were able to enhance sampling
186 conformations from MD trajectories.

187

188 **Integrin affinity measurements**
189 Next, we directly measured integrin affinity for the well-characterized Fab fragment, Wow-1,
190 whose RGD-dependent binding to αvβ3 increases dramatically after activation (25). Wow1 is
191 monomeric, minimizing possible effects of integrin clustering on its binding. Cells expressing
192 WT or mutant αvβ3 were incubated with Wow-1 in standard, Mg^{2+}- and Ca^{2+} -containing buffer
193 or in the presence of Mn^{2+}, which is commonly used as a positive control for maximal activation
194 (34). αvβ3-null cells were used as a negative control. We found that in Ca^{2+}/Mg^{2+}, all of the
195 point mutants showed significantly increased binding compared to WT, with no significant

6

196 differences detected among the activated mutants (Figure 7). Further, the activating mutants
197 showed no further increase in the presence of Mn^{2+}. This last result implies that all of the
198 mutants are maximally activated in these assays.
199
200 **CG simulations reveal intermediate states**
201 In all of our CG simulations, the integrin headpiece extended away from the legs, with the degree
202 of extension depending on the mutant examined and the threshold of removed or converted
203 harmonic interactions. Snapshots from a representative simulation of S243E, with springs
204 preserved for $k > 0.1$ kcalmol^{-1}A^2, are shown in Figure 8. We next computed the RMSD of the
205 simulated systems for all of the single point mutants relative to the four cryo-EM structures (24).
206 In particular, we looked at the configurations of wild type and mutant integrins that were closest
207 to each cryo-EM structure, using the minimum RMSD from CG trajectories, RMSD$_{MIN}$, and
208 compared how much they differed. Our results showed that for $k > 0.001$ kcalmol^{-1}A^2, the single
209 mutants deviate from the cryo-EM conformer more than the WT in the following cases: closed
210 (Figure 9a) and first intermediate (Figure 9b) and open conformer (Figure 9d) cryo-EM. With
211 respect to the second intermediate from the cryo-EM conformer, the mutant systems generally
212 have higher RMSD$_{MIN}$ than the WT for $k > 0.0001$ kcalmol^{-1}A^2. The comparison of our CG
213 mutants with full-length cryo-EM conformers from single molecule experiments show
214 surprisingly strong structural similarity. This indicates that the simulations are consistent with a
215 deadbolt model for integrin opening and inconsistent with the switchblade mechanism.
216 Furthermore, the simulations show that this opening mechanism results from weakening low
217 stiffness long-range correlations while preserving local dynamics correlations within each
218 integrin subdomain and between pairs of neighboring subdomains along the primary protein
219 sequence.
220
221

222   **DISCUSSION**

223

224   In this study, we have addressed how integrin headpiece extension coordinates with leg
225   separation during integrin opening. We utilized a novel combination of AA MD simulation, ED-
226   CG modeling, and a modified heteroENM approach that allows for large conformational change
227   on single and double point mutants of full-length $\alpha_V\beta_3$ integrin. We investigated whether
228   destabilization of the closed conformation occurs as localized structural rearrangements or as
229   more cooperative changes in the receptor headpiece and legs. Also, we used ligand binding
230   experiments and comparison of our CG models with single molecule cryoEM integrin
231   reconstructions to validate our modeling configurations.

232

233   The AA MD simulations, albeit of limited large-scale sampling, showed that β3 mutations
234   induce molecular structural rearrangements in both headpiece and legs of α and β subunits. In
235   mutants, these rearrangements are generally enhanced relative to wild type integrins, by initiation
236   of headpiece opening, flattening of the kink angle, and separation of the transmembrane helices
237   (Figure 3). All mutants here analyzed destabilize the linkers within the α and β subunits,
238   including Linker 1 and the EGF motifs (Figure 2b-c, e-f), respectively. The effect of mutants on
239   linkers could facilitate structural transition towards open states. This result is in agreement with
240   previous data from MD simulations on the EGF- motifs of the β subunit single cysteine
241   mutations (35). These studies suggested that rearrangement of disulfide bonds in mutants could
242   be part of a cascade of thiol/disulfide exchange reactions for activation (35). Results from our
243   AA MD simulations also reveal that while structural properties of the systems do not converge
244   within 1 μs (Figure S1 and Figure S3), the mutants that maximally destabilize the closed state are
245   S243E and D723R (Figure S4). The hydrophilic surface area is known to be significantly larger
246   for S243E compared to wild type αvβ3 and other mutants. This reflects greater extension of the
247   headpiece away from the lipid bilayer, flattening of both kink angles and initiation of separation
248   of transmembrane helices (Figure 3c and Figure S4). The effect of S243E on the global structural
249   reorganization of integrin is triggered by the formation of a salt bridge at the point of the
250   mutation, which induced local reorientation of a histidine, aspartic acid and arginine (Figure 4).
251   In the case of the double mutant D723R_S243E, a salt bridge still forms in the βA domain
252   (Figure S6), but the altered electrostatic interactions induced by mutation of aspartic acid to
253   arginine in the β transmembrane helix and its higher pKa generate more stable interactions
254   within the two helices (Figure S7).

255

256   The result that a single mutation in the βA domain of the β subunit can initiate structural opening
257   is consistent with a number of previous MD studies of the integrin headpiece. For example,
258   simulations of fibronectin-bound integrin headpiece showed that the ligand binding pocket at the
259   interface between α and β subunits together with the hinge between the βA and hybrid domain of
260   the β subunit are allosterically linked to initiate opening (18). In MD simulations of both $\alpha_{IIb}\beta_3$
261   and $\alpha_V\beta_3$ integrin headpieces, a common transition pathway for propagation of conformational
262   changes within the βA domain was identified as the precursor of structural opening (36),
263   consistent with our results from modified heteroENM that opening of the βA/hybrid junction can
264   act as a hinge. Molecular simulations of the integrin headpiece were also previously performed
265   in combination with experimental headpiece mutation to show that reorientation of the hybrid
266   domain in the β subunit is required for structural activation (37). Forced unbending of the
267   integrin αvβ3 headpiece was simulated using SMD, which showed that pulling the head readily

8

268 induced changes starting from the headpiece (38). This supports that headpiece extension is very
269 critical in integrin opening. In the current study, we used the full-length atomistic receptor
270 which, unlike previous efforts, allowed us to characterize motional correlations between
271 headpiece and legs and to further detect the impact of short versus long range correlations on
272 integrin extension. With this study, we were also able to analyze the effect of the D723R
273 mutation in the cytoplasmic tail of the β subunit, showing that propagation of structural
274 activation can also be reproduced in this mutant.
275
276 In order to set our MD results into a broader context and test whether headpiece extension and
277 leg separation are correlated at longer time scales, we used multiscale CG methods on individual
278 integrins (with effect of lipid bilayer implicitly included in the AA MD input), based on ED-CG
279 and HeteroENM methods, which were developed in (32, 33). This approach reduced the number
280 of integrin sites from 27215 to 200, and reduced the computational cost by >100-fold. We
281 modified our standard heteroENM model so that it can undergo large scale conformational
282 changes by systematically removing low stiffness springs or converting them into softer,
283 dissociable Morse interactions to facilitate realistic conformational flexibility. The predictive
284 validity of standard ED-CG-hENM approaches was therefore significantly extended to enable
285 sampling of multiple integrin conformations outside of the AA MD used to parameterize aspects
286 of the model.
287
288 Results from the CG simulations confirmed that all mutants destabilized the integrin closed
289 conformation via enhancement of kink angles and persistence of open configurations (Figure 6).
290 This result was consistent with the experimental finding that WOW-1 binding was maximal for
291 all of the mutants examined (Figure 7). However, this maximal activation for all mutants
292 obscures possible differences. Dynamic measurements that are sensitive to the kinetics of
293 activation will be an interesting target for future studies.
294
295 We also compared our αvβ3 CG structures with cryo-EM reconstructions of αIIbβ3 integrins at
296 different states of activation, which had observed headpiece extension before leg separation (24).
297 Integrin extension in the CG models resulted from preserving local atomistic dynamics
298 correlations within each integrin subdomain and between pairs of neighboring subdomains along
299 the primary protein sequence, while removing weak molecular long-range correlations. This
300 suggests that, in the case of limited sampling, certain correlations present in the AA MD
301 simulations were not representative of correlations in the global conformational landscape.
302
303

CONCLUDING REMARKS

Our results from AA MD simulations show that coordinated atomistic motions within and between headpiece and legs destabilize integrin closed conformation on time scales on the order of μs (8). However, at longer time scales, accessed via CG simulations, headpiece extension precedes leg separation. Also, this activation mechanism for αvβ3 integrin is consistent with recent cryo-EM reconstructions of $\alpha_{IIb}\beta_3$ integrin (20). In our simulations, extension of the headpiece occurs upon reduction of heteroENM effective harmonic interaction connectivity by maintaining connections within and between consecutive subdomains and modifying the low-frequency connections between distant subdomains. This implies that local contacts can persist during integrin opening and that long-range, low-frequency motional correlations are not consistent between closed and extended integrin states. Our model therefore supports the notion integrin extension results from disruption of weak, long-range interactions. In order for the legs to move apart in the model, stronger correlations between non-consecutive subdomains should also be reduced in the CG model, but this would lead to an overall loss of structural integrity and not only legs separation. Stated differently, our model is inconsistent with a switchblade mechanism.

To conclude, the main findings from this study are: (1) point mutations in the β subunit destabilize the αvβ3 closed structure in the absence of extracellular or intracellular ligands; (2) in the mutants, both integrin headpiece and legs respond to destabilization of the closed configuration via transmission of conformational transitions through flexible linkers; (3) the S243E mutant is an "activating" mutation that acts not only on the integrin headpiece but also allosterically on the transmembrane helices at the molecular level; and (4) headpiece extension can occur before leg separation, similar to cryo-EM reconstructions and consistent with a deadbolt model of integrin activation (Figure 8 and Figure 9).

Our findings of more general relevance are the following. Motions induced by integrin distal parts, that are weakly correlated at the atomistic level, leads to increased structural flexibility in full-length integrin and can thus promote extension. This motion can be induced experimentally in WT integrin by extracellular ligand binding or intracellular binding of the cytoskeletal protein talin, that bind the receptor in distal locations. Extracellular or intracellular integrin binding proteins can thus modify weakly correlated interactions between distal subdomains of the receptor, while preserving stronger, local correlations within subdomains and between neighboring subdomains. The idea of preserving collective local motions for integrin structural activation points towards a view of the receptor as sensitive in conformation to changes of weak, long-range inter-domains interactions.

10

344   **MATERIALS AND METHODS**

345

346   In order to characterize integrin conformational activation, we computationally reconstructed
347   full-length $\alpha_V\beta_3$ integrins embedded in a lipid bilayer. We mutated the WT conformer using
348   single or double point activating mutations in the βA domain of the β subunit, in the
349   transmembrane β helix or in both. We tested whether initiation of integrin opening is, on the
350   timescale of $1\mu s$, a local effect, involving only the headpiece or the legs, or a global
351   phenomenon, with simultaneous structural rearrangements in both the headpiece and the legs.
352   Then, we built coarse-grained models of each integrin system to sample a wider range of
353   conformations and test correlations between headpiece extension and leg separation over longer
354   times. With both MD and CG simulations, we tested which activating mutations favor structural
355   opening. This result was verified with experiments using the monovalent ligand WOW-1Fab
356   (25), which direct assesses $\alpha_V\beta_3$ affinity state. Last, we compared our CG conformations with
357   available cryo-EM reconstructions of $\alpha_{IIb}\beta_3$ integrin, which is closely related to $\alpha v\beta 3$ (24).

358

359   **All-atom simulations**

360   To examine the effect of mutation on the conformation of full length integrin $\alpha_V\beta_3$, μs length all–
361   atom molecular dynamics (AA MD) simulations were performed on the integrins embedded in a
362   lipid square patch (see Figure 1b). We assembled the bent headpiece of $\alpha_V\beta_3$ integrin [from
363   3IJE.pdb (26)] with its transmembrane helical and cytoplasmic parts [taken from 2KNC.pdb
364   (27)], using homology modeling to reconstruct missing residues (28). Point mutations were
365   selected based on studies that identified mutants that increased affinity for RGD ligands (12).
366   Starting from this initial configuration, we used the VMD software (29) to build five single
367   mutants and four double mutants: D723R, L138I, E206T, S243E, K417E, D723R-L138I,
368   D723R-E206T, D723R-S243E and D723R-K417E. For each integrin, we generated a
369   multicomponent model lipid bilayer with 80% DOPC and 20% DOPS lipids, using CHARMM-
370   GUI membrane builder (30). We then removed lipids in the center of the lipid patch to make a
371   hole and inserted the integrin (Figure 1b). Last, we placed the membrane/integrin system within
372   a rectangular box and filled its space with TIP3P water molecules and 150 mM NaCl, for a total
373   of about 1.2 million atoms. In order to reorganize the lipids around the integrin, energy
374   minimization was run for 5000 steps of steepest decent algorithm, followed by 50 ns of position
375   restraint in a constant NPT ensemble, using the Berendsen thermostat. Production AA MD
376   simulation were carried out, using Gromacs 5.0.4 (31), for $1\mu s$ in the NPT ensemble using Nose-
377   Hoover thermostat and Parrinello-Rahman barostat to keep the temperature at 310 K and
378   pressure at 1 atm. Long-range electrostatic interactions were incorporated through the PME
379   method with a cut-off of 1 nm. The same cut-off value was used for Lennard-Jones interactions.

380

381   In order to identify differences in headpiece versus leg arrangements between WT integrin and
382   the mutants, we defined metrics that report both headpiece extension and legs separation (Figure
383   3a). We quantified the following: kink angles, ϑ_1 and ϑ_2, for α and β subunits, respectively; their
384   average, ϑ; transmembrane legs separation; D_{12}, and headpiece extension, D_{EM} (see schematics in
385   Figure 3A). The angle ϑ_1 was defined in the α subunit as the angle between points A1 (center of
386   mass of residues 82-85 in the β-propeller domain), A2 (center of mass of residues 599-602,
387   between tight domain and Linker 1) and A3 (center of mass of restudies 963-966 in the α
388   transmembrane helix); for the β subunit, ϑ_2 was defined as the angle between points B1 (center of

389   mass of residues 236-239 in the βA domain), B2 (center of mass of residues 480-484, between
390   the hybrid domain and the EGF-1/EGF-2 motifs) and B3 (center of mass of restudies 696-699 in
391   the β transmembrane helix); E is a point at the interface between the two headpiece subunits and
392   was defined as the center of mass between points A1 and B1; M was defined as the center of
393   mass between points A3 and B3 (corresponding residues are 963-966 and 696-699 in the two
394   helices); points A and B, whose distance was indicated with D_{12}, were given by the midpoints of
395   each transmembrane helix.

396

397   **Coarse-grained model**
398   In order to fully become active, integrins must sample multiple intermediate conformational
399   states (24). Many of these conformational states were not accessed by AA MD simulations
400   owing to the relatively short timescales that can be sampled at that level. We therefore built CG
401   models based on the observed motional correlations of atoms in MD simulations and used them
402   to identify structural differences between the WT and mutants on effectively longer timescales.
403   We first developed Essential Dynamics Coarse-graining (ED-CG) (32) and heterogeneous elastic
404   network (HeteroENM) models (33) of each integrin starting from the AA MD trajectories
405   (without explicit inclusion of the lipid membrane in these model-it is there in the AA MD data,
406   however). The ED-CG approach was chosen in order to select CG sites which preserve
407   independent motion in the CG protein, and because it is constructed from the primary protein
408   sequence without distorting it when exploring a wide conformational space. The heteroENM
409   approach was used to create effective harmonic interactions between the CG sites which directly
410   capture nanoscale correlations from the AA MD simulations. This approach was critical for
411   creating CG models that maintain molecular differences between the integrin mutants studied
412   here.

413

414   However, our present application of ED-CG and heteroENM differs from previous studies in one
415   important and novel way. In previous applications of ED-CG and heteroENM, the elastic
416   network was created to replicate all fluctuation dynamics observed in the reference AA MD
417   simulations (32, 33). Here, certain correlations present in the MD simulations only provide a
418   glimpse of the larger scale changes in the global conformational landscape, because of their
419   limited sampling. In order for the CG model to sample substantially beyond the observed
420   reference AA MD configurations, the hENM procedure was modified in this work by reducing
421   the effective harmonic connectivity of each hENM integrin as a model for large conformation
422   changes. We either systematically removed a varying fraction of the effective harmonic
423   potentials or converted some of the inter-domain harmonic interactions into "softer" Morse
424   potentials. In particular, we modified only those inter-domain interactions between non-
425   consecutive subdomains along the subunits in order to maintain connections along the primary
426   sequence of the proteins. We tested conditions where harmonic interaction potentials with
427   equilibrium stiffness $k < 0.0005$-0.1 kcalmol^{-1}A^2 were modified, using 200 CG sites and an
428   enforced cutoff 3 nm for each integrin. By modifying a fraction of harmonic potentials with k
429   below 0.0005 kcalmol^{-1}A^2, no significant structural reconfiguration of the receptor was observed.
430   By increasing the upper limit above 0.1 kcalmol^{-1}A^2, structural connectivity was lost. Upon
431   performing CG dynamics on these systems, we evaluated their conformational motion in order to
432   characterize whether destabilization of the closed integrin conformer occurs in a coordinated
433   fashion between headpiece and legs, and detect which mutants most effectively destabilized the

434 closed conformation. Last, we compared our CG trajectories with mapped cryo-EM
435 reconstructions of $\alpha_{IIb}\beta_3$ integrin intermediates (24).
436

Cell Lines
438 Mouse lung endothelial cells (MLECs) were isolated from β3 integrin null mice. β3 integrin
439 single point mutants were generously provided by Timothy Springer (Harvard University) and
440 Mark Ginsberg (UCSD). Double mutants were constructed by standard site directed
441 mutagenesis. These sequences were subcloned into pBOB vector and virus prepared in HEK
442 293Tx cells by co-transfecting with pCMV-VSV-G and psPAX2 using Lipofectamine 2000
443 (Invitrogen). The temperature sensitive mutant of the SV40 virus large T antigen was employed
444 for conditional immortalization of these cells. Immortalized β3-/- MLECs were infected with
445 wild-type (WT) or mutant β3 integrin viruses and subsequently sorted to obtain homogenous
446 populations with equal expression levels. For expansion, MLECs were cultured in 1:1 Hams F-
447 12 and low glucose DMEM with 20% FBS, 1% Penicillin-Streptomycin, 2.5mM glutamine and
448 endothelial cell growth supplement (ECGS, 50mg/L) at the permissive temperature of 30°C. For
449 experiments, cells were switched to 37°C to inactivate large T one day prior.
450

Integrin activation measurements
452 To measure integrin affinity state, cells were detached using 0.25% trypsin, washed with
453 complete medium, resuspended in serum-free medium at 13.3×10^6 cells/mL, and incubated with
454 primary β3-specific integrin ligands and secondary antibodies at 4×10^5 cells in 50 µL as
455 described (34). Briefly, to assess surface expression of β3, cells were incubated with 7H2
456 primary antibody (Developmental Studies Hybridoma Bank), washed with DMEM, incubated
457 with anti-mouse-Alexafluor-647 secondary antibody (Invitrogen), washed with DMEM, and
458 resuspended in PBS. To assess β3 activation state, cells were incubated with WOW-1 primary
459 Fab (generously provided by S. Shattil) in the presence or absence of 20 mM EDTA or 2 mM
460 MnCl$_2$, washed with DMEM, incubated with secondary F(ab')2 anti-mouse IgG (H+L)
461 Alexafluor-488 (Invitrogen), washed with DMEM, and resuspended in PBS. Primary antibody
462 was omitted to assess background fluorescence. Fluorescence was measured on an LSRII flow
463 cytometer (BD Biosciences). The β3-integrin activation index of cells was calculated as AI = (F -
464 Fo)/Fintegrin, where F is the geometric mean fluorescence intensity (MFI) of WOW-1 binding
465 after background subtraction, Fo is the MFI of WOW-1 binding in presence of EDTA inhibitor,
466 and Fintegrin is the normalized MFI of 7H2 antibody binding to cells. Activation was
467 normalized to WT under native conditions for 4 independent experiments.
468
469

470 **ACKNOWLEDGEMENTS**

471

REFERENCES

1.   Hood, J.D., and D.A. Cheresh. 2002. ROLE OF INTEGRINS IN CELL INVASION AND MIGRATION. Nat. Rev. Cancer. 2: 91–100.

2.   Bershadsky, A.D., N.Q. Balaban, and B. Geiger. 2003. Adhesion-Dependent Cell Mechanosensitivity. Annu. Rev. Cell Dev. Biol. 19: 677–695.

3.   Ingber, D.E. 2003. Mechanobiology and diseases of mechanotransduction. Ann Med. 35: 1–14.

4.   Ross, T.D., B.G. Coon, S. Yun, N. Baeyens, K. Tanaka, M. Ouyang, and M.A. Schwartz. 2013. Integrins in mechanotransduction. Curr. Opin. Cell Biol. 25: 613–8.

5.   Vogel, V., and M. Sheetz. 2006. Local force and geometry sensing regulate cell functions. Nat. Rev. Mol. Cell Biol. 7: 265–275.

6.   Banno, A., and M.H. Ginsberg. 2008. Integrin activation. Biochem. Soc. Trans. 36: 229–234.

7.   Carman, C. V, and T.A. Springer. 2003. Integrin avidity regulation: are changes in affinity and conformation underemphasized? Curr. Opin. Cell Biol. 15: 547–56.

8.   Luo, B.-H., C. V Carman, and T.A. Springer. 2007. Structural basis of integrin regulation and signaling. Annu. Rev. Immunol. 25: 619–47.

9.   Ye, F., C. Kim, and M.H. Ginsberg. 2012. Reconstruction of integrin activation. Blood. 119: 26–33.

10. Hynes, R.O. 2002. Integrins: bidirectional, allosteric signaling machines. Cell. 110: 673–87.

11. Campbell, I.D., and M.J. Humphries. 2011. Integrin Structure, Activation, and Interactions. Cold Spring Harb. Perspect. Biol. 3: a004994–a004994.

12. Luo, B.-H., J. Karanicolas, L.D. Harmacek, D. Baker, and T.A. Springer. 2009. Rationally designed integrin beta3 mutants stabilized in the high affinity conformation. J. Biol. Chem. 284: 3917–24.

13. Luo, B.-H., T.A. Springer, and J. Takagi. 2003. Stabilizing the open conformation of the integrin headpiece with a glycan wedge increases affinity for ligand. Proc. Natl. Acad. Sci. U. S. A. 100: 2403–8.

14. Luo, B.-H., K. Strokovich, T. Walz, T.A. Springer, and J. Takagi. 2004. Allosteric NL 1 Integrin Antibodies That Stabilize the Low Affinity State by Preventing the Swing-out of the Hybrid Domain*. .

15. Xie, C., J. Zhu, X. Chen, L. Mi, N. Nishida, and T.A. Springer. 2010. Structure of an integrin with an αI domain, complement receptor type 4. EMBO J. 29: 666–679.

16. Xiao, T., J. Takagi, B.S. Coller, J.-H. Wang, and T.A. Springer. 2004. Structural basis for allostery in integrins and binding to fibrinogen-mimetic therapeutics. Nature. 432: 59–67.

17. Huth, J.R., E.T. Olejniczak, R. Mendoza, H. Liang, E.A. Harris, M.L. Lupher, A.E. Wilson, S.W. Fesik, D.E. Staunton, and D.E. Staunton. 2000. NMR and mutagenesis evidence for an I domain allosteric site that regulates lymphocyte function-associated antigen 1 ligand binding. Proc. Natl. Acad. Sci. U. S. A. 97: 5231–6.

18. Puklin-Faucher, E., M. Gao, K. Schulten, and V. Vogel. 2006. How the headpiece hinge angle is opened: new insights into the dynamics of integrin activation. J. Cell Biol. 175: 349–360.

19. Mehrbod, M., S. Trisno, and M.R.K. Mofrad. 2013. On the activation of integrin αIIbβ3: outside-in and inside-out pathways. Biophys. J. 105: 1304–15.

15

523 20. Adair, B.D., J.-P. Xiong, C. Maddock, S.L. Goodman, M.A. Arnaout, and M. Yeager.
524   2005. Three-dimensional EM structure of the ectodomain of integrin {alpha}V{beta}3 in
525   a complex with fibronectin. J. Cell Biol. 168: 1109–18.

526 21. Mould, A.P., S.J. Barton, J.A. Askari, P.A. McEwan, P.A. Buckley, S.E. Craig, and M.J.
527   Humphries. 2003. Conformational changes in the integrin beta A domain provide a
528   mechanism for signal transduction via hybrid domain movement. J. Biol. Chem. 278:
529   17028–35.

530 22. Zhu, J., J. Zhu, and T.A. Springer. 2013. Complete integrin headpiece opening in eight
531   steps. J. Cell Biol. 201.

532 23. Arnaout, M.A., S.L. Goodman, and J.-P. Xiong. 2007. Structure and mechanics of
533   integrin-based cell adhesion. Curr. Opin. Cell Biol. 19: 495–507.

534 24. Xu, X.-P., E. Kim, M. Swift, J.W. Smith, N. Volkmann, and D. Hanein. 2016. Three-
535   Dimensional Structures of Full-Length, Membrane-Embedded Human α(IIb)β(3) Integrin
536   Complexes. Biophys. J. 110: 798–809.

537 25. Pampori, N., T. Hato, D.G. Stupack, S. Aidoudi, D.A. Cheresh, G.R. Nemerow, and S.J.
538   Shattil. 1999. Mechanisms and consequences of affinity modulation of integrin
539   alpha(V)beta(3) detected with a novel patch-engineered monovalent ligand. J. Biol. Chem.
540   274: 21609–16.

541 26. Xiong, J.-P., B. Mahalingham, J.L. Alonso, L.A. Borrelli, X. Rui, S. Anand, B.T. Hyman,
542   T. Rysiok, D. Müller-Pompalla, S.L. Goodman, and M.A. Arnaout. 2009. Crystal structure
543   of the complete integrin αVβ3 ectodomain plus an α/β transmembrane fragment. J. Cell
544   Biol. 186: 589–600.

545 27. Yang, J., Y.-Q. Ma, R.C. Page, S. Misra, E.F. Plow, and J. Qin. 2009. Structure of an
546   integrin alphaIIb beta3 transmembrane-cytoplasmic heterocomplex provides insight into
547   integrin activation. Proc. Natl. Acad. Sci. U. S. A. 106: 17729–34.

548 28. Pettersen, E.F., T.D. Goddard, C.C. Huang, G.S. Couch, D.M. Greenblatt, E.C. Meng, and
549   T.E. Ferrin. 2004. UCSF Chimera?A visualization system for exploratory research and
550   analysis. J. Comput. Chem. 25: 1605–1612.

551 29. Humphrey, W., A. Dalke, and K. Schulten. 1996. VMD: Visual molecular dynamics. J.
552   Mol. Graph. 14: 33–38.

553 30. Jo, S., J.B. Lim, J.B. Klauda, and W. Im. 2009. CHARMM-GUI Membrane Builder for
554   Mixed Bilayers and Its Application to Yeast Membranes. Biophys. J. 97: 50–58.

555 31. Abraham, M.J., T. Murtola, R. Schulz, S. Páll, J.C. Smith, B. Hess, and E. Lindah. 2015.
556   Gromacs: High performance molecular simulations through multi-level parallelism from
557   laptops to supercomputers. SoftwareX. 1–2: 19–25.

558 32. Zhang, Z., L. Lu, W.G. Noid, V. Krishna, J. Pfaendtner, and G.A. Voth. 2008. A
559   Systematic Methodology for Defining Coarse-Grained Sites in Large Biomolecules.
560   Biophys. J. 95: 5073–5083.

561 33. Lyman, E., J. Pfaendtner, and G.A. Voth. 2008. Systematic multiscale parameterization of
562   heterogeneous elastic network models of proteins. Biophys. J. 95: 4183–92.

563 34. Bouaouina, M., D.S. Harburger, and D.A. Calderwood. 2011. Talin and Signaling
564   Through Integrins. In: Methods in molecular biology (Clifton, N.J.). . pp. 325–347.

565 35. Levin, L., E. Zelzion, E. Nachliel, M. Gutman, Y. Tsfadia, and Y. Einav. 2013. A Single
566   Disulfide Bond Disruption in the β3 Integrin Subunit Promotes Thiol/Disulfide Exchange,
567   a Molecular Dynamics Study. PLoS One. 8: e59175.

568 36. Provasi, D., M. Murcia, B.S. Coller, and M. Filizola. 2009. Targeted molecular dynamics

569   reveals overall common conformational changes upon hybrid domain swing-out in β3
570   integrins. Proteins Struct. Funct. Bioinforma. 77: 477–489.
571   37.   Cheng, M., J. Li, A. Negri, B.S. Coller, and L.R. Languino. 2013. Swing-Out of the b3
572   Hybrid Domain Is Required for aIIbb3 Priming and Normal Cytoskeletal Reorganization,
573   but Not Adhesion to Immobilized Fibrinogen. .
574   38.   Chen, W., J. Lou, J. Hsin, K. Schulten, S.C. Harvey, and C. Zhu. 2011. Molecular
575   Dynamics Simulations of Forced Unbending of Integrin αVβ3. PLoS Comput. Biol. 7:
576   e1001086.
577
578

579   **FIGURES**

580
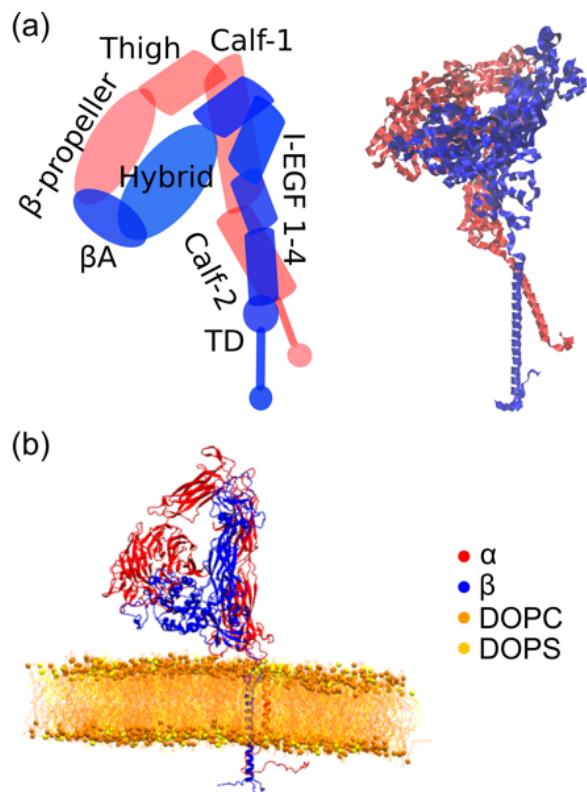
581

582   **Figure 1. Structures of full length, closed $\alpha_{IIb}\beta_3$ and $\alpha_V\beta_3$ integrins and corresponding**
583   **molecular models**. (a) Structure of $\alpha_{IIb}\beta_3$ integrin in its closed, low affinity conformation.
584   Subunits α and β are represented in red and blue, respectively. Corresponding ribbon
585   representation of closed $\alpha_{IIb}\beta_3$ integrin on the right (from (24)). (b) Ribbon representation of
586   atomistic full-length $\alpha_V\beta_3$ integrin embedded in DOPC/DOPS (4:1) lipid bilayer.

587

588
589
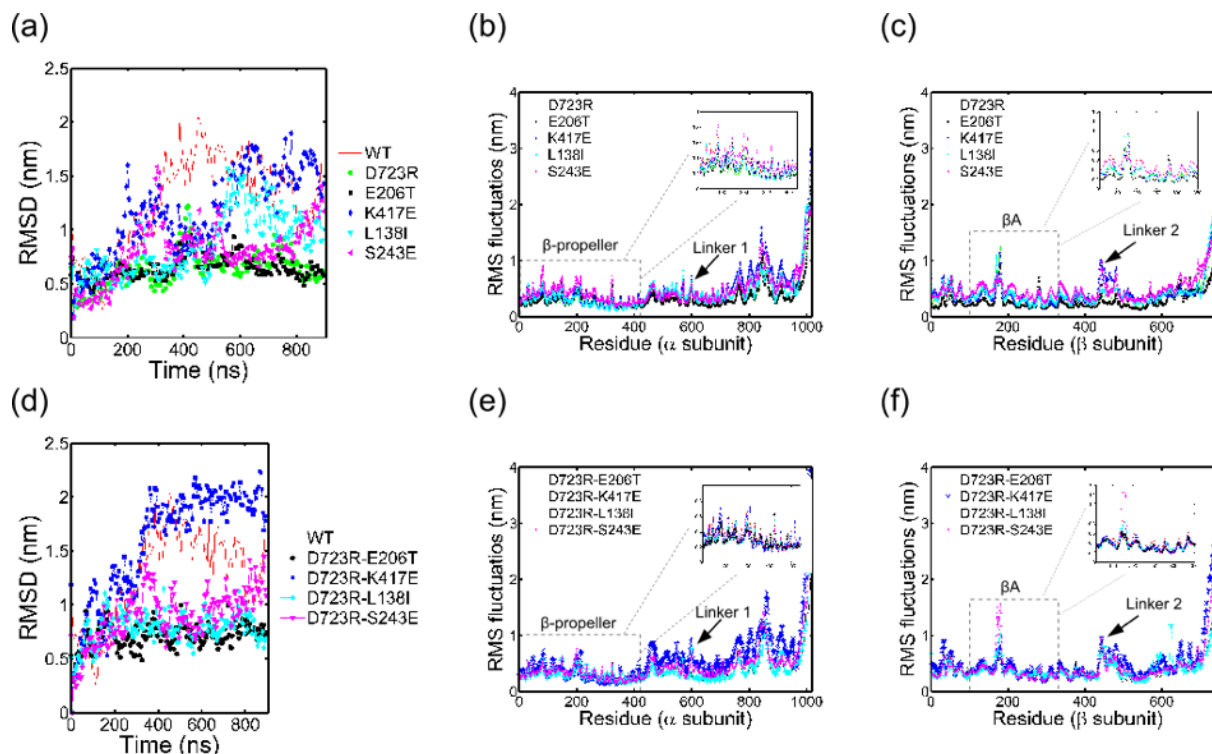
590
591 **Figure 2. All atom molecular dynamics simulations of integrin αvβ3 mutants.** (a) Time
592 evolution of root mean square deviations of the atomistic C_α for WT and single integrin mutants
593 relative to the corresponding equilibrated configurations used as input to the MD. (b) Root mean
594 square fluctuations of individual residues in the α subunit of WT and single integrin mutants. (c)
595 Root mean square fluctuations of individual residues in the α subunit of WT and single integrin
596 mutants. Color code in (a), (b), and (c) is: WT (red), D723R (green), E206T (black), K417E
597 (blue), L138I (cyan), S243E (magenta). (d) Time evolution of root mean square deviations of the
598 atomistic C_α for WT and double integrin mutants relative to the corresponding equilibrated
599 configurations given as input to the MD. (e) Root mean square fluctuations of individual residues
600 in the α subunit of WT and double integrin mutants. (f) Root mean square fluctuations of
601 individual residues in the α subunit of WT and double integrin mutants. Color code in (d), (e),
602 and (f) is: WT (red), D723R-E206T (black), D723R-K417E (blue), D723R-L138I (cyan),
603 D723R-S243E (magenta).

19

604
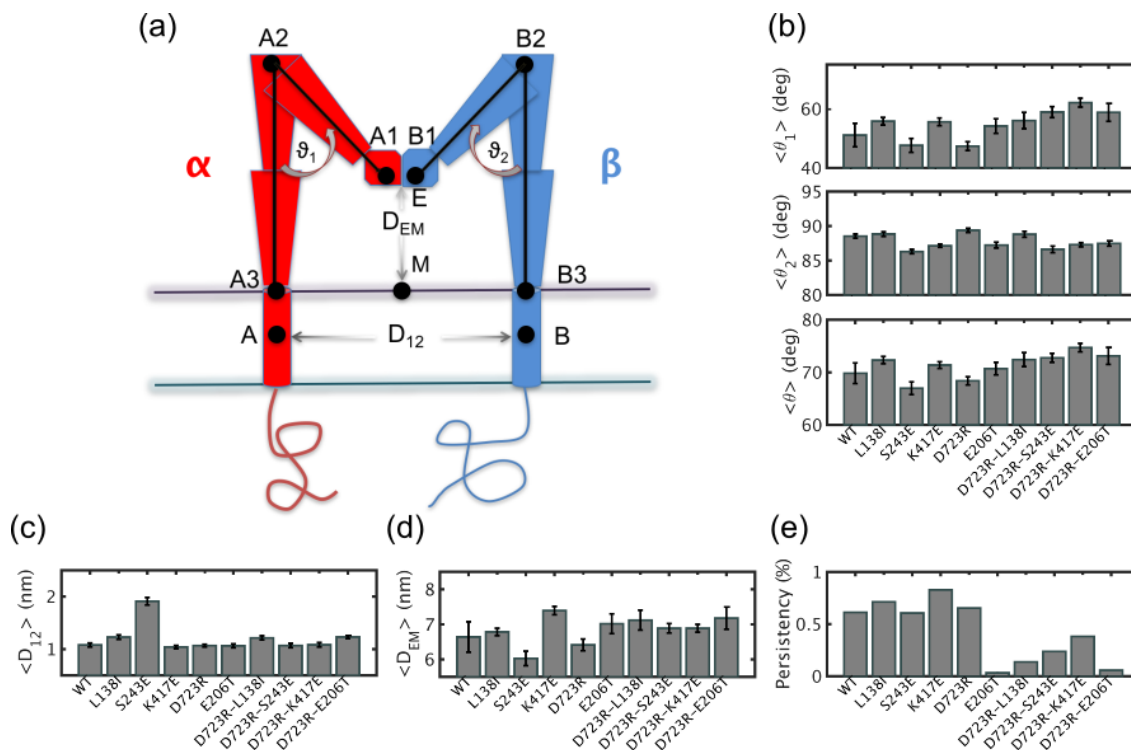
605
606 **Figure 3. Leg separation, headpiece extension and kink angles in the last 100 ns of AA MD**
607 **simulations.** (a) Schematic diagram of αvβ3 in a lipid bilayer membrane, with red and blue
608 elements representing α and β subunits, respectively. The horizontal lines indicate upper and
609 lower membrane leaflets. Points A1, A2, A3 on the α subunit and points B1, B2, B3 on the β
610 subunit are used to characterize corresponding kink angles, ϑ_1 and ϑ_2. Distance D_{12} indicates
611 separation between the two transmembrane helices and D_{EM} is a measure of headpiece extension
612 from the membrane. (b) Average values of ϑ_1, ϑ_2 and ϑ in WT and mutant integrins, computed
613 between 900-1000 ns of MD simulations. (c) Average values of D_{12} in WT and mutant integrins.
614 (d) Average values of D_{EM} in WT and mutant integrins. (e) Persistence of extended state for WT
615 and mutant integrins, computed as the fraction of time, between 900-1000nm of MD, that D_{EM}
616 was at least 95% of its maximum value

617
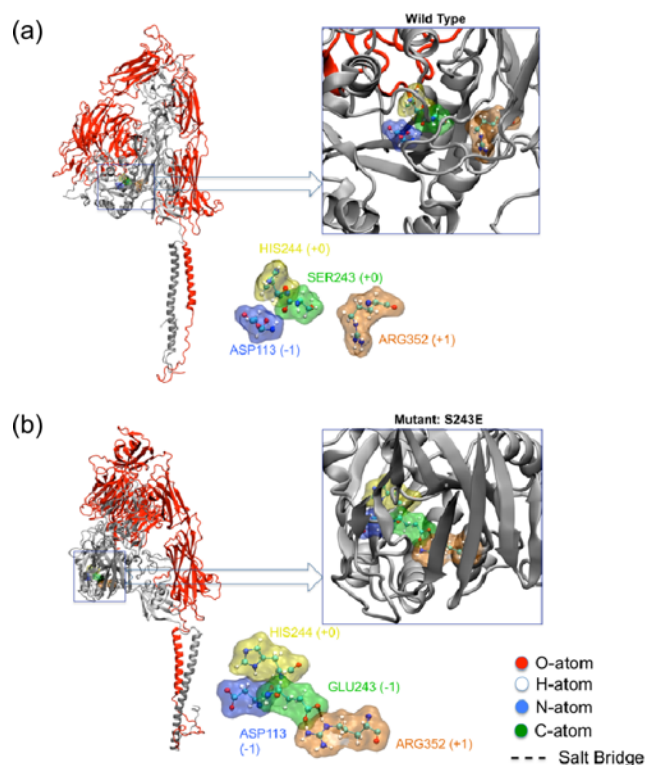
618
619 **Figure 4. S243E triggers formation of a salt bridge in the βA domain of β subunit.** (a)
620 Cartoon representation of full length WT integrin with α subunit in red and β subunit in grey.
621 Highlighted and zoomed are the amino acids surrounding S243 (green): histidine (yellow),
622 aspartic acid (violet) and arginine (orange) (b). Cartoon representation of full length mutant
623 integrin with α subunit in red and β subunit in grey. Highlighted and zoomed are the amino acids
624 surrounding mutated S243E, using the same color code as in (a). Dashed line shows a salt bridge
625 between negative Glu243 and positive Arg352. Oxygen, hydrogen, nitrogen and carbon atoms
626 are shown in ball and stick representation in red, white, blue and green, respectively.

627
628
629
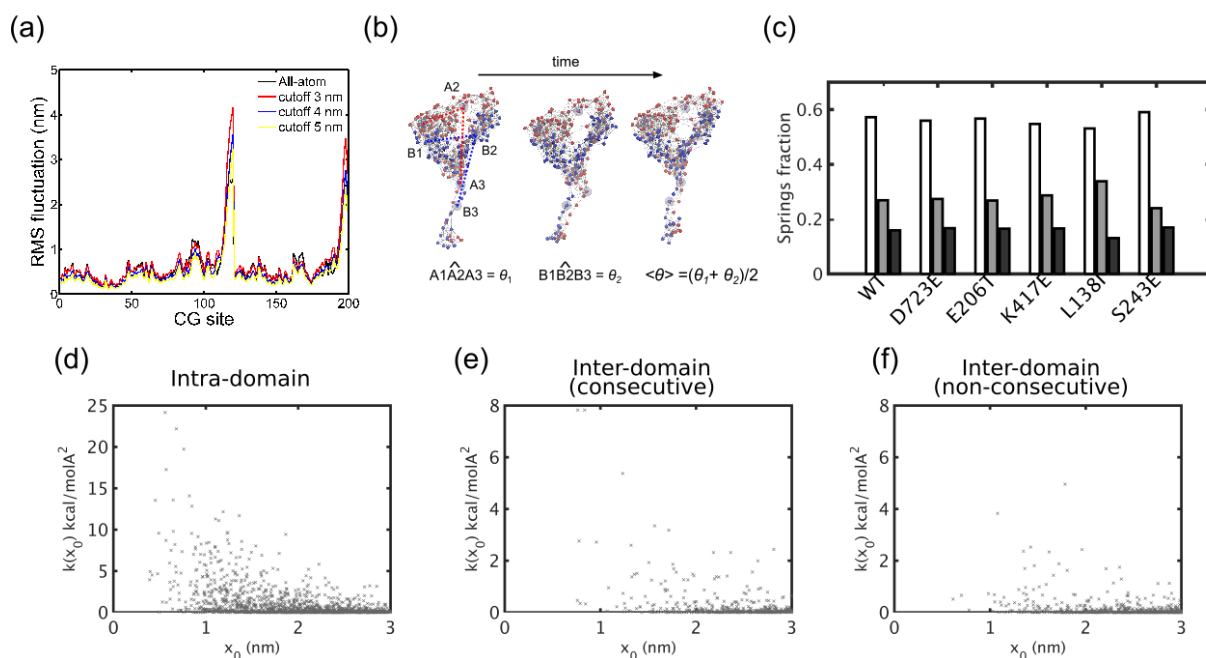
630
631 **Figure 5. ED-CG-heteroENM models of integrin mutants.** (a) Per-CG-site root mean square
632 fluctuations of WT integrin computed from AA MD simulations and ED-CG-heteroENM
633 integrin using cutoffs of 3, 4, and 5 nm. (b) Snapshots from CG-heteroENM S243E integrin
634 simulations, with red indicating CG-sites of the α subunit and blue indicating CG-sites of the β
635 subunit. Bonds represent harmonic interactions. CG-sites representing A1, A2, A3 and B1, B2,
636 B3 are mapped from atomistic residues. (c) Fraction of harmonic interactions from hetero-ENM,
637 for WT and single mutant integrins: interactions within each domain (white); between
638 consecutive subdomains along the primary aminoacidic sequence (grey), and between non-
639 consecutive subdomains (black). (d) Spring constants of intra-domain interactions between CG-
640 sites, as a function of equilibrium lengths x_0 for heteroENM D723R. (e) Spring constants for CG-
641 sites of consecutive subdomains, versus x_0 for heteroENM D723R. (f) Spring constants of CG-
642 sites of non-consecutive subdomains, as a function of x_0 for heteroENM D723R.

22

(a)

(b)
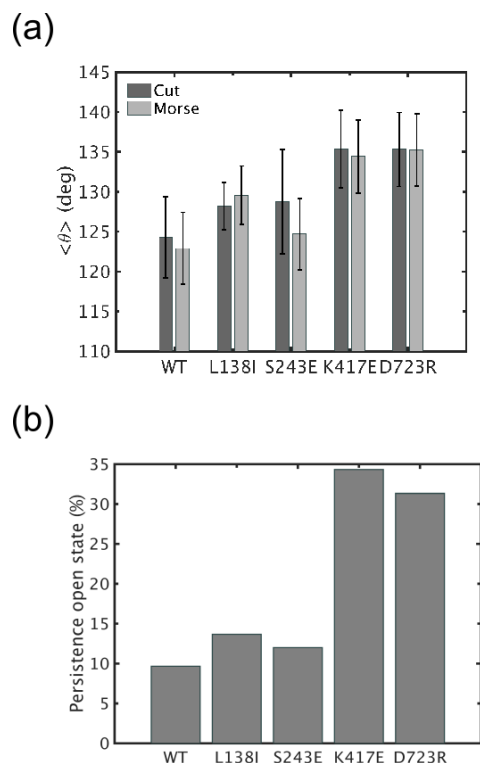
Figure 6. CG simulations of integrin mutants. (a) Average kink angle computed as mean of ϑ_1 and ϑ_2 over the course of the CG simulations, using WT and single mutant integrin with elastic springs above a threshold ($k\,(x_0) > 0.005$ kcalmol^{-1}A^2) and either cut (eliminated) springs or soft Morse potentials below the threshold. (b) Persistence of the integrin open state, computed as the percentage of simulation time during which integrin has D_{EM} above 95%, its maximum value (results for cut springs above $k\,(x_0) > 0.1$ kcalmol^{-1}A^2).

23
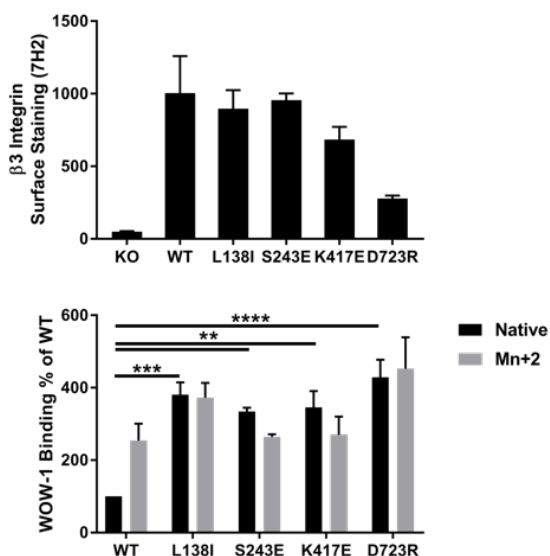
Figure 7. Integrin activation assays. $\alpha_v\beta_3$ activation was assayed experimentally by binding of the monomeric, ligand-mimetic Fab, WOW-1. β3 integrin knockout cells expressing wild type or mutant β3 in suspension were stained Alexa647-conjugated antibody 7H2 that binds to all $\alpha_v\beta_3$, and with Alexa488-conjugated WOW-1 by flow cytometry (~ 500k cells per condition). Binding of WOW-1 was normalized to the average total β3 integrin (a). Binding was performed under native, EDTA, and Mn^{+2} conditions. WOW-1 binding is shown relative to WT in native conditions (b). Values are means ± SEM, n=4 independent experiments. (** $p < 0.01$, *** $p < 0.001$, **** $p<0.0001$, Two-way ANOVA with Sidak's multiple comparisons test)

24

662
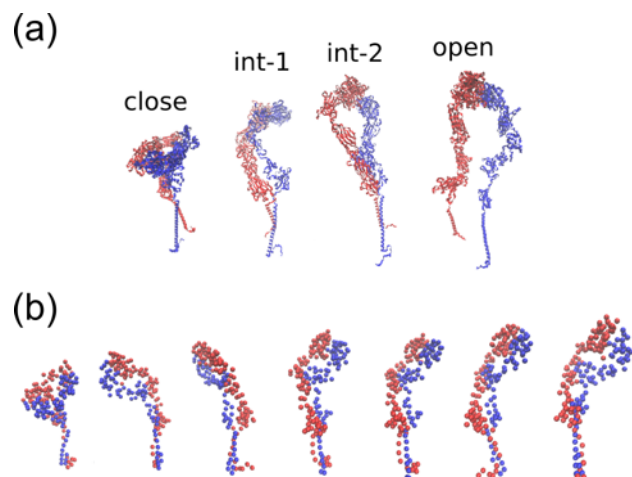
663
664 **Figure 8. CG models show that headpiece extension occurs without legs separation**. (a)
665 reconstructed configurations form cryo-EM (24): closed; first intermediate; second intermediate
666 and open conformers. (b) Representative snapshots from CG simulations of S243E with cut
667 springs below $k(x_0) = 0.1$ kcalmol^{-1}A^2, showing extension of the closed conformer.
668

669
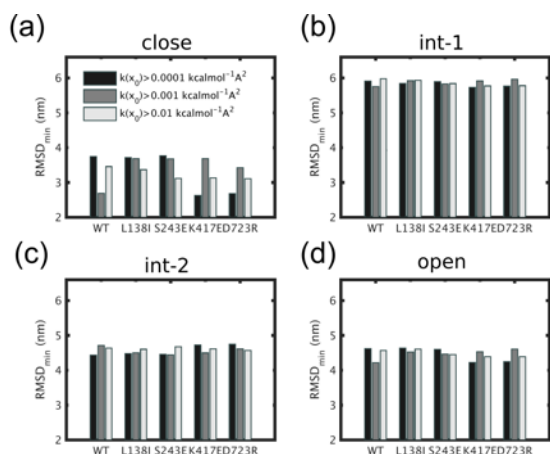
Figure 9. Comparison of CG-heteroENM structures with cryo-EM reconstructions of closed, intermediate and open integrins (a) Minimum RMSD between CG-heteroENM simulations and the closed conformer. (b) Minimum RMSD between CG-heteroENM simulations and the first integrin intermediate. (c) Minimum RMSD between CG-heteroENM simulations and second integrin intermediate. (d) Minimum RMSD between CG-heteroENM simulations and open integrin conformer.

676